Effect of three-dimensional propagation characteristics on the horizontal array gain in wedge-shaped transitional water

Jinci Wang(王谨辞), Bo Lei(雷波), Yixin Yang(杨益新), Jianbo Zhou(周建波)
Citation: Chin. Phys. B. 35, 104303 (2026). DOI: 10.1088/1674-1056/ae9c21 | CSTR: 32038.14.CPB.ae9c21
http://cpb.iphy.ac.cn; http://iopscience.iop.org/cpb

What follows is a list of articles you may be interested in

Acoustic propagation uncertainty in internal wave environments using an ocean-acoustic joint model

Fei Gao(高飞), Fanghua Xu(徐芳华), Zhenglin Li(李整林), Jixing Qin(秦继兴), Qinya Zhang(章沁雅)
Chin. Phys. B. 32, 034302 (2023). DOI: 10.1088/1674-1056/ac89dc

Effects of mesoscale eddies on the spatial coherence of a middle range sound field in deep water

Fei Gao(高飞), Fang-Hua Xu(徐芳华), Zheng-Lin Li(李整林)
Chin. Phys. B. 31, 114302 (2022). DOI: 10.1088/1674-1056/ac6014

Effect of the fluctuant acoustic channel on the gain of a linear array in the ocean waveguide

Lei Xie(谢磊), Chao Sun(孙超), Guang-Yu Jiang(蒋光禹), Xiong-Hou Liu(刘雄厚), De-Zhi Kong(孔德智)
Chin. Phys. B. 27, 114301 (2018). DOI: 10.1088/1674-1056/27/11/114301

Spatial correlation of the high intensity zone in deep-water acoustic field

Jun Li(李鋆), Zheng-Lin Li(李整林), Yun Ren(任云)
Chin. Phys. B. 25, 124310 (2016). DOI: 10.1088/1674-1056/25/12/124310

Effect of three-dimensional propagation characteristics on the horizontal array gain in wedge-shaped transitional water

Jinci Wang(王谨辞)[1,2], Bo Lei(雷波)[1,2,†], Yixin Yang(杨益新)[2,3], and Jianbo Zhou(周建波)[1,2]

[1] *School of Marine Science and Technology, Northwestern Polytechnical University, Xi'an* 710072, *China*
[2] *Shaanxi Key Laboratory of Underwater Information Technology, Northwestern Polytechnical University, Xi'an* 710072, *China*
[3] *School of Electronic and Optical Engineering, Nanjing University of Science and Technology, Nanjing* 210094, *China*

(Received 18 June 2026; revised manuscript received 18 August 2026; accepted manuscript online 20 August 2026)

Array gain is the fundamental determinant of the detection performance of large-aperture arrays in applications for long-range underwater target detection. However, field experiments conducted on the continental slope of the South China Sea reveal significant discrepancies between measured and theoretical array gains. To quantitatively explain this phenomenon, this study derives an array gain expression based on the exponential–cosine coherence model, which provides a coherent physical interpretation of the effects of three-dimensional (3D) propagation characteristics on array gain. Using a rigorous controlled-variable approach, we quantitatively isolate the independent contributions of the three core spatial coherence parameters (coherent amplitude coefficient A, spatial coherence attenuation coefficient γ, and spatial oscillation angular frequency κ) and element signal energy E_i to array gain. The analysis demonstrates that, in wedge-shaped sloping environments, bathymetric variability induces horizontal divergence of acoustic energy, which leads to degradation of horizontal spatial coherence and ultimately results in array performance degradation. Incomplete accounting for the horizontal energy divergence effect inherent in 3D propagation systematically overestimates the coherence amplitude coefficient A — the dominant factor determining array gain — and thus leads to significant array gain underestimation. The theoretical analysis is experimentally validated using field measurement data from eight sites across the study area. The derived array gain expression accurately reproduces the experimentally observed array gain behavior, with excellent quantitative agreement between theoretical model calculations and experimental results. As a result, the normalized mean squared error is less than 0.08 at all measurement sites. The agreement between the calculated and experimental array gains supports the proposed mechanism analysis. The consistent results across the eight sites also indicate that the identified relationships among 3D propagation, spatial coherence, and array gain apply throughout the investigated continental slope region.

Keywords: continental slope, horizontal correlation, horizontal array gain performance

PACS: 43.60.Fg, 91.50.Bd, 82.20.Sb

DOI: 10.1088/1674-1056/ae9c21 **CSTR:** 32038.14.CPB.ae9c21

1. Introduction

Array gain, as a quantifiable measure of the improvement in array processing gain over a single receiver, is affected by acoustic propagation characteristics in waveguide environments. In a pioneering study, Bourret[1] established the quantitative relationship between environmental variability and array performance. Subsequent early investigations of array gain primarily focused on random perturbations in signal amplitude and phase.[2–4] Following the work of Berman and Berman,[2] who derived the mean array output power under Gaussian phase fluctuations, Brown[3] further obtained a closed-form solution for the variance of the array output. Importantly, Carey[5] derived the formula for calculating array gain based on spatial functions and obtained the relationship between array gain and coherence length. This research direction has provided theoretical foundations and practical guidance for optimizing the deployment of acoustic arrays in realistic ocean environments.

Building on these theoretical foundations, numerous experimental studies have been conducted to characterize spatial coherence and array performance in diverse oceanographic settings. Dong *et al.*[6] investigated the intrinsic relationship between spatial coherence of the acoustic field and vertical array gain in the deep-sea environment. Through theoretical derivation and experimental validation, their work revealed that the attenuation of vertical coherence constitutes the physical mechanism leading to the degradation of array gain. Based on the SW06 experimental data, Duda *et al.*[7] have demonstrated that horizontal refraction induced by internal waves can significantly degrade spatial coherence in flat continental shelf environments. The investigated environment had an average water depth of approximately 80 m and seabed slopes of less than 0.1°. Xie *et al.*[8–10] employed the parabolic equation (PE) model to analyze acoustic field characteristics during upslope propagation in a two-dimensional (2D) continental slope environment.

As previous studies identified spatial coherence as the primary factor governing array gain, research on spatial coher-

†Corresponding author. E-mail: lei.bo@nwpu.edu.cn

© 2026 Chinese Physical Society and IOP Publishing Ltd. All rights, including for text and data mining, AI training, and similar technologies, are reserved.

ence has attracted increasing attention. These investigations of spatial coherence have systematically characterized the spatial coherence properties in different typical marine environments: shallow water,[11–18] continental slopes,[7–10,19–21] and the deep sea.[6,22] Existing works have further quantified how environment-specific factors shape spatial coherence. In shallow water, spatial coherence is dominated by multimode interference and boundary interactions.[9] Continental slopes exhibit anisotropic coherence due to three-dimensional (3D) horizontal refraction,[21] whereas deep-sea coherence shows strong seasonal variations driven by internal waves and surface scattering.[22] High-order Bragg forward scattering from a moving rough sea surface can also produce frequency shifts in low-frequency underwater acoustic fields.[23] In addition, multiple methods[24,25] have been proposed to enhance array gain by improving signal correlation.

Although previous studies have established fundamental links between ocean environments and spatial coherence, important areas for further exploration remain. The 2022 paper by Lin *et al.*[21] focused on the experimental verification of 3D sound propagation mechanisms. These authors focused exclusively on sound field characteristics such as transmission loss and arrival structure and did not explore their quantitative impact on array gain and beamforming performance. Meanwhile, analyses of continental slope array gain[8–10] were based on 2D models, which ignored the horizontal refraction-induced coherence degradation that is prevalent in wedge-shaped environments. To address these critical knowledge gaps, this study systematically investigates the underlying mechanisms by which 3D acoustic propagation characteristics affect large-aperture horizontal array gain in wedge-shaped continental slope environments.

To investigate the effects of 3D acoustic propagation characteristics on array gain in continental slope environments, this study develops theoretical analysis, numerical simulations, and validation using experimental data from eight sites in the South China Sea. This work derives an array gain expression based on the exponential–cosine coherence model, which demonstrates that bathymetric variability induces horizontal divergence of acoustic energy. This condition leads to degradation of horizontal spatial coherence and ultimately results in array performance degradation in wedge-shaped sloping environments.

The paper is organized as follows. First, the significance of large-aperture horizontal arrays for target detection in wedge-shaped shallow-water environments is emphasized. Second, we present the field experiment data from the continental shelf-slope region of the South China Sea. Transmission loss of experimental data and models are compared. Third, we establish the array gain formulation based on the normalized signal correlation coefficient model. The next section employs the controlled-variable method to analyze the independent contributions of three spatial coherence parameters and element energy, which is verified by comparing measured data from eight sites with model array gain. In the final section, the conclusion is written.

2. Experimental configuration and model validation

The sound propagation experiment was conducted in the South China Sea by the Shaanxi Key Laboratory of Underwater Information Technology in August 2025. The experimental site is located in the continental shelf-slope transition zone, with a fixed-inclination linear upslope of 3°. As shown in Fig. 1, the water depth decreases from 700 m to 400 m along the 6 km upslope propagation path. The bathymetric map delineates the fixed location of the sound source and the trajectory of the receiving array. Eight discrete measurement stations (S1–S8) along the receiving-array trajectory were selected for acoustic data acquisition.

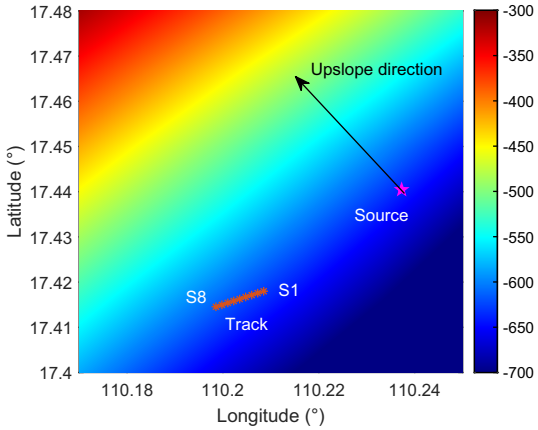

Fig. 1. Bathymetric map of the experimental area and the experimental configuration.

To accurately describe the 3D acoustic propagation environment, a Cartesian coordinate system is defined as illustrated in Fig. 2. Figure 2(a) shows the *YZ* cross-section of the wedge-shaped slope. A horizontal receiving array is towed by a surface vessel at a depth z_r, while the acoustic source is suspended at a fixed depth z_s beneath the sea surface. The seabed, which is characterized by a uniform inclination angle α, constitutes a wedge-shaped acoustic boundary that governs ray refraction and modal coupling.

Figure 2(b) presents the *XY* horizontal cross-section. The coordinate origin ($x = 0$, $y = 0$) is located vertically above the acoustic source. Consistent with the coordinate system defined in Fig. 2(a), the source is positioned at (0, 0, z_s). The *y*-axis is aligned with the upslope direction, which corresponds to the direction of decreasing water depth. The *x*-axis is orthogonal to the *y*-axis, and the water depth remains constant along the *x*-axis. The receiving array takes the element nearest to the

towing vessel as its reference element. The azimuth angle ϕ represents the angle between the array axis and the radial direction from the source to the reference element. Specifically, $\phi = 0^\circ$ indicates that the array is oriented along the positive x-axis, whereas $\phi = 90^\circ$ indicates that the array is oriented along the positive y-axis. The array location angle $\bar{\theta}$ is defined as the angle between the line segment connecting the acoustic source to the reference array element and the positive y-axis direction, which is expressed as

$$\bar{\theta} = \arctan\left(\frac{x_{\mathrm{r}}}{y_{\mathrm{r}}}\right), \tag{1}$$

In the experimental system, a 60 Hz continuous-wave sound source was deployed at a depth of 30 m in the deeper water region. The receiving system was an 84-element unequally spaced horizontal line array (HLA) towed at a depth of 50 m, which operated at a sampling frequency of 32 kHz. The detailed inter-element spacing of the array is presented in Fig. 3. During the experiment, the source ship remained stationary while the receiver ship towed the HLA along the track shown in Fig. 1. Acoustic data were collected continuously as the receiving array moved from a source–receiver range of 4 km to 5.5 km. The station-related data recorded during the experiment are listed in Table 1. The continuously collected data enabled high-resolution characterization of the effects of 3D acoustic propagation on array gain.

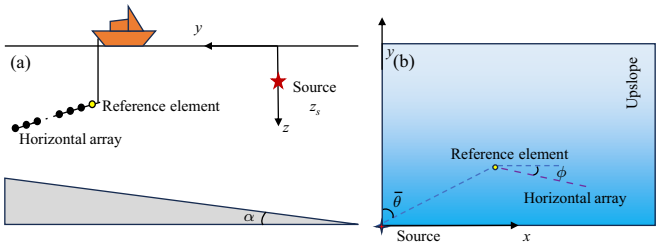

Fig. 2. Diagram of the wedge-shaped slope. (a) *YZ* cross-section of the wedge-shaped slope; (b) *XY* cross-section of the wedge-shaped slope.

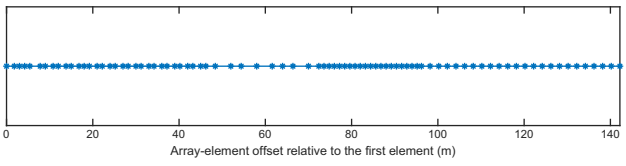

Fig. 3. Schematic diagram of experimental configuration. The horizontal axis denotes the offset of each array element relative to the first element.

During the experiment, a conductivity–temperature–depth (CTD) profiler was deployed to measure the in situ hydrographic conditions of the experimental area. The sound speed profile of the seawater was calculated using the classical sound speed formula, as shown in Fig. 4(a). To satisfy the requirements of the sound field simulation, the sound speed profile was vertically extended to 700 m by assimilating climatological data from the World Ocean Atlas (WOA), which yielded the sound speed profile shown in Fig. 4(b). The parameters for the bottom sediment include a sound speed of 1700 m/s, an absorption coefficient of 0.5 dB/λ, and a density of 1.5 g/cm^3.

Table 1. Experimental receiving station parameters.

Site number	Source–receiver range (m)	Array depth (m)	Array location angle $\bar{\theta}$ (°)	Array heading angle ϕ (°)
S1	4266.2	63.5	81.5	31.5
S2	4402.1	63.8	81.1	31.7
S3	4540.5	64.8	80.7	31.5
S4	4677.2	64.6	80.3	31.8
S5	4815.9	64.5	80.0	31.7
S6	4952.9	64.1	79.6	31.6
S7	5088.9	64.7	79.3	31.3
S8	5227.0	64.7	79.0	31.6

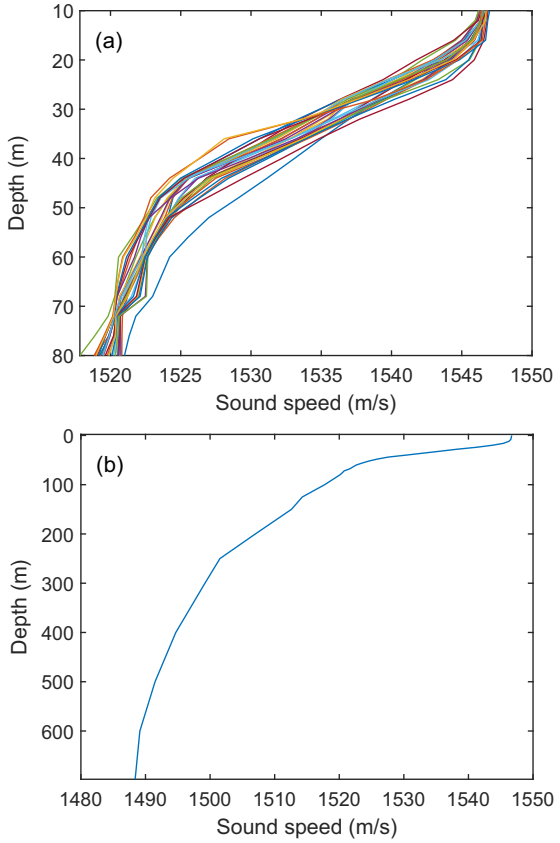

Fig. 4. Sound speed profiles. (a) In situ measured profiles from CTD data; (b) extended profile to 700 m using WOA climatological data for sound field simulation.

The time-domain received signals recorded by the large-aperture horizontal array at the eight experimental sites are shown in Fig. 5. Each subplot presents the waveforms from five representative array elements (elements 1, 20, 40, 60, and 84) over a 2.5 s observation window. The received signals exhibit distinct temporal characteristics across different sites, with variations in arrival time and signal amplitude.

To quantitatively evaluate the prediction fidelity of different propagation models, we conducted two sets of comparative simulations under the identical environmental conditions of

the field experiment: one fully incorporating 3D propagation effects and the other neglecting them. The three-dimensional finite element (3D FE) model fully resolves all 3D propagation effects, including cross-slope mode coupling and the horizontal divergence of acoustic energy. The sound pressure field is obtained by solving the Helmholtz equation with appropriate sea surface and seabed boundary conditions, with the mesh size set to one-fifth of the acoustic wavelength at the operating frequency to ensure numerical accuracy. By contrast, the $N\times$2D PE model was adopted to handle the range-dependent bathymetry and low-frequency (60 Hz) propagation characteristics. This model assumes azimuthal symmetry and neglects horizontal mode coupling between different propagation directions.

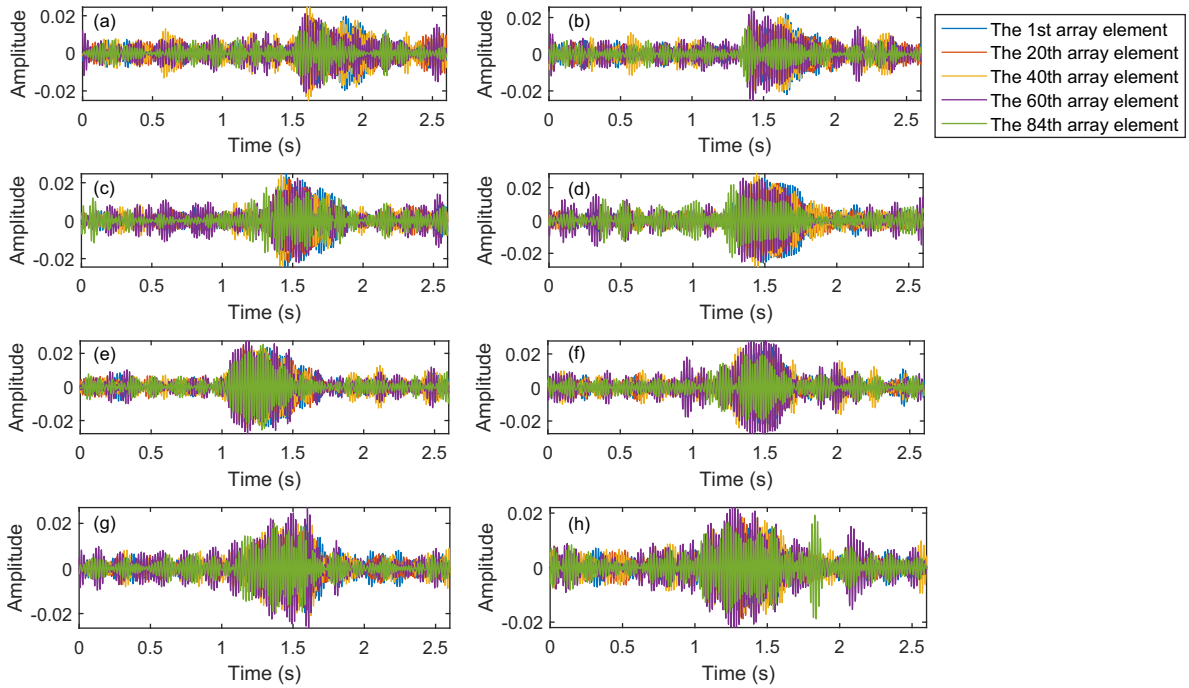

Fig. 5. Received signal waveforms recorded by the large-aperture horizontal array at eight experimental sites. (a)–(h) correspond to Sites S1–S8, respectively. Each subplot displays the waveforms from five representative array elements (elements 1, 20, 40, 60, and 84).

The complex pressure of the i-th element of the non-uniform horizontal array is p_i ($i = 1,2,3,\ldots,N$, and N is the number of array elements). The coordinate vector of the i-th array element is $\boldsymbol{r}_i = (x_i, y_i)$, and x_i and y_i are the horizontal and vertical coordinates of the array elements on the horizontal plane, respectively.

In the field data processing and numerical simulations, the acoustic energy within the 55–65 Hz band was averaged to represent the effective level at the center frequency of 60 Hz. To facilitate comparison of large-scale propagation trends over long ranges while minimizing source-level errors, normalized transmission loss (NTL) was employed. The NTL is calculated by

$$\mathrm{NTL}(\boldsymbol{r}) = -20 \times \log_{10}\left(\sum_{\omega_\mathrm{L}}^{\omega_\mathrm{H}} |p(\boldsymbol{r},\omega)|^2 \Big/ \max_{\boldsymbol{r}}\left(\sum_{\omega_\mathrm{L}}^{\omega_\mathrm{H}} |p(\boldsymbol{r},\omega)|^2\right)\right), \quad (2)$$

where ω_L and ω_H denote the lower and upper limits of the angular frequency, respectively. ω denotes an angular-frequency sample. The horizontal correlation coefficient ρ_{in} between the i-th and n-th elements is defined as

$$\rho(\Delta r_{in}) = \frac{\langle p_i p_n^* \rangle}{\sqrt{\left\langle |p_i|^2 \right\rangle}\sqrt{\left\langle |p_n|^2 \right\rangle}}, \quad (3)$$

where the symbol $\langle\cdot\rangle$ denotes the statistical average, and $*$ indicates the conjugate operation. $\Delta\boldsymbol{r}_{in}$ indicates the range between the i-th and n-th elements.

Figure 6 compares the NTL across eight localized regions within the 4–5 km propagation range. The 3D FE model faithfully reproduces the global trend and fluctuations of the measured NTL at all eight observation stations. The reproduced features include trough locations, relative amplitudes, and phase-aligned oscillatory behavior. By contrast, the model neglecting the 3D propagation characteristics, which omits the coupling between vertical topographic variation and horizontal acoustic propagation, yields excessively smoothed NTL and exhibits consistent trend-level bias. Thus, it fails to represent the physically rich, energy-distributed dynamics observed in field measurements.

As illustrated in Fig. 7, the array gain versus the number of array elements is computed from the measured sound-pressure data at all eight experimental sites using the conven-

tional beamforming (CBF) algorithm. Across all sites, array gain increases with the number of elements. However, it is significantly lower than the ideal array gain of $10\lg(N)$, where N is the array number. In continental slope environments, the multipath propagation effects induced by range-dependent bathymetry cause the received signals to no longer satisfy the plane wave assumption. This condition results in degraded spatial coherence and subsequent array gain reduction.

Array gain presents the capability of an array to enhance the signal relative to ambient noise. The spatial coherence characteristics of ambient noise therefore play a critical role in governing array performance, and the validity of underlying noise field assumptions fundamentally determines the accuracy of subsequent array gain analyses. To accurately characterize the ambient noise properties in the experimental area, pure ambient noise data were acquired during periods of target signal silence, calm sea surface conditions, and the absence of nearby vessel activity. For the narrowband operating band of 55–65 Hz examined in this study, the normalized spatial coherence coefficients between all element pairs were computed and are presented in Fig. 8.

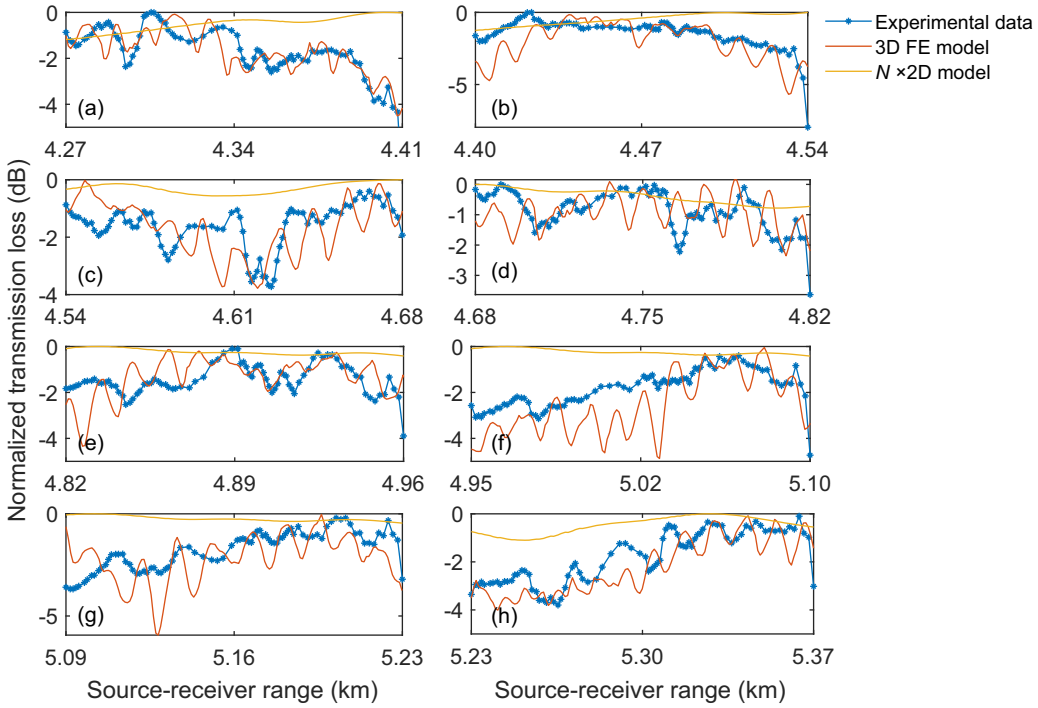

Fig. 6. Comparison of normalized transmission loss versus source–receiver range at the eight measurement sites: (a) S1, (b) S2, (c) S3, (d) S4, (e) S5, (f) S6, (g) S7, and (h) S8. The blue curve with markers represents the experimental data, the red curve represents the 3D FE model, and the yellow curve represents the $N\times$2D model.

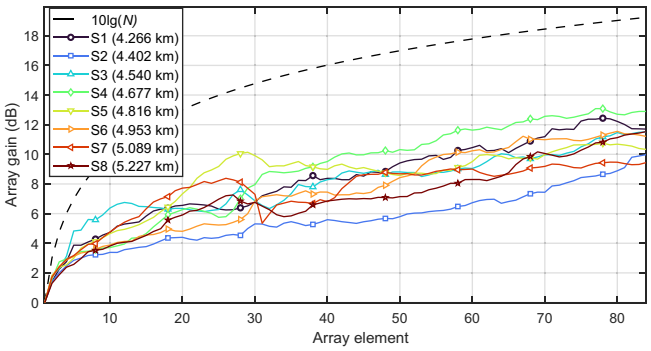

Fig. 7. Measured array gain as a function of the number of array elements at Sites S1–S8. The black dashed curve represents the ideal $10\lg(N)$ array gain, where N is the number of array elements. The measured array gain generally increases with the number of elements.

As shown in Fig. 8, the normalized spatial coherence coefficient of the ambient noise decays rapidly to near zero over a relatively short inter-element spacing range. Crucially, this coefficient remains at a low level with small oscillations across the full aperture of the 84-element horizontal array employed in the experiment.

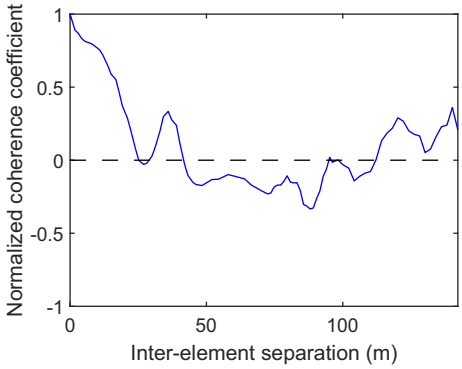

Fig. 8. Normalized spatial coherence coefficient of ambient noise at the experimental site during the experiment as a function of the inter-element separation.

This experimental observation agrees well with the theoretical spatial coherence characteristics of an isotropic ho-

mogeneous noise field. This agreement supports the validity of the isotropic noise assumption for the specific continental slope environment and the 55–65 Hz narrowband considered in this study. Consequently, this assumption is adopted throughout all subsequent theoretical derivations and array gain performance analyses.

3. Basical theory and relative parameters

The continental slope, which is a transitional zone connecting the deep sea with shallow waters, provides a strategic location for a horizontal array to enable target detection and bearing estimation. However, the complex 3D acoustic propagation effects induced by the changing terrain in this area complicate array gain modeling.

3.1. Wedge-shaped slope model

The Helmholtz equation for acoustic pressure $p(x,y,z)$ due to a point source is

$$\nabla^2 p(x,y,z) + k^2(z)\, p(x,y,z) = 0, \tag{4}$$

where $\nabla^2 = \frac{\partial^2}{\partial x^2} + \frac{\partial^2}{\partial y^2} + \frac{\partial^2}{\partial z^2}$ indicates the Laplacian operator, and $k(z) = 2\pi f / c(z)$ is the wavenumber that only varies with depth z, and f is the frequency. $c(z)$ is the sound speed in water.

Based on the continuity conditions of sound pressure and particle velocity at the seafloor boundary, pressure $p(x,y,z)$ should satisfy the following:

$$p|_{z=H^-} = p|_{z=H^+}, \quad \frac{1}{\rho_1}\frac{\partial}{\partial \hat{\boldsymbol{n}}}\, p|_{z=H^-} = \frac{1}{\rho_2}\frac{\partial}{\partial \hat{\mathrm{n}}}\, p|_{z=H^+}, \tag{5}$$

where ρ_1 and ρ_2 indicate the densities of the water and bottom layer, respectively.

For a horizontally homogeneous environment with a flat seafloor, the 3D Helmholtz equation can be decomposed into multiple independent vertical 2D (x–z plane) Helmholtz equations through the method of separation of variables. In this case, the transverse (y-direction) acoustic pressure gradient term $\partial^2 p/\partial y^2 = 0$. This serves as the theoretical foundation of the conventional $N\times$2D approximation. For the wedge-shaped slope environment in this study, the seabed depth $H(y)$ varies with the horizontal coordinate y, and the boundary conditions change with the propagation distance. The acoustic pressure gradient term $\partial^2 p/\partial y^2$ cannot be eliminated, which leads to acoustic energy coupling along the horizontal direction.

3.2. CBF array gain based on the exponential–cosine spatial correlation model

Assuming that a farfield narrowband signal is impinging on the horizontal array, the complex sound pressure received by the ith element can be expressed as

$$p_i = A_i \exp\left(-\mathrm{j}k\boldsymbol{u}(\theta_0)^{\mathrm{T}}\boldsymbol{r}_i\right), \tag{6}$$

where A_i is the amplitude of the i-th element, and j denotes the imaginary unit. $\boldsymbol{u}(\theta_0) = (\cos\theta_0, \sin\theta_0)$ denotes the unit wavevector pointing in the direction of signal incidence, and θ_0 denotes the direction of arrival of the incident signal. T denotes the transpose operation.

CBF is adopted as the array processing method in this study, as it requires no prior information and exhibits exceptional robustness. This choice ensures that the observed variations in array gain fully reveal the effects of 3D acoustic propagation. The array steering vector of CBF is

$$w(\theta) = \left[\mathrm{e}^{\mathrm{j}k\boldsymbol{u}(\theta)^{\mathrm{T}}\boldsymbol{r}_1}, \mathrm{e}^{\mathrm{j}k\boldsymbol{u}(\theta)^{\mathrm{T}}\boldsymbol{r}_2}, \cdots, \mathrm{e}^{\mathrm{j}k\boldsymbol{u}(\theta)^{\mathrm{T}}\boldsymbol{r}_N}\right]^{\mathrm{T}}, \tag{7}$$

where θ denotes the array steering angle. The beamformer output $p_{\mathrm{out}}(\theta)$, which is defined as the weighted sum of the acoustic pressure signals received, is expressed as

$$p_{\mathrm{out}}(\theta) = \sum_{i=1}^{N} w_i(\theta) p_i, \tag{8}$$

where N is the total number of array elements. The average output power of the beamformer is

$$P_{\mathrm{out}} = \left\langle |p_{\mathrm{out}}|^2 \right\rangle = \left\langle \left| \sum_{i=1}^{N} w_i p_i \right|^2 \right\rangle = \sum_{i=1}^{N}\sum_{n=1}^{N} w_i w_n^* \left\langle p_i p_n^* \right\rangle. \tag{9}$$

Let $E_i = \left\langle |p_i|^2 \right\rangle$ denote the statistical average of the acoustic energy received by the i-th array element. Array gain (AG), which is an important parameter for evaluating array performance, is defined as the signal-to-noise ratio improvement of an array compared with a single hydrophone. Building on the measured ambient noise spatial coherence results, we employ the isotropic ambient noise assumption in the array gain derivation. The array gain of CBF[10] is written as

$$\begin{aligned} \mathrm{AG} &= 10\lg\left(\frac{S_{\mathrm{array}}}{N_{\mathrm{array}}} \Big/ \frac{S_{\mathrm{avg}}}{N_{\mathrm{avg}}}\right) \\ &= 10\lg\left(\frac{\sum_{i=1}^{N}\sum_{n=1}^{N} \rho(\Delta r_{in})\sqrt{E_i E_n}}{E_{\mathrm{tot}}}\right), \end{aligned} \tag{10}$$

where $E_{\mathrm{tot}} = \sum_{i=1}^{N} E_i$. S_{array} and N_{array} are the beamformer output powers of the signal and noise, respectively. S_{avg} and N_{avg} are the array average powers of the signal and noise, respectively. Δr_{in} denotes the distance between the i-th and n-th elements.

The conventional single-exponential model characterizes a monotonic decrease in spatial coherence with increasing element separation. It can provide a reasonable approximation of the overall trend when spatial coherence generally decreases with increasing element separation. However, in the wedge-shaped slope environment considered in this study, modal and multipath interference may introduce spatial oscillations superimposed on the overall coherence decay. Similar oscillatory decay characteristics have also been reported in Ref. [10].

Accordingly, the exponential–cosine spatial coherence model is adopted, and the normalized spatial coherence coefficient[4] can be expressed as

$$\rho(\Delta r_{in}) = A\exp(-\gamma\Delta r_{in})\cos(\kappa\Delta r_{in}) + (1-A), \quad (11)$$

where $\rho(\Delta r_{in})$ is the dimensionless normalized spatial coherence coefficient. The parameter $A \in (0,1]$ is the dimensionless coherent amplitude coefficient and controls the relative contribution of the oscillatory component. The parameter $\gamma > 0$, expressed in m^{-1}, is the spatial coherence attenuation coefficient. The parameter $\kappa > 0$, expressed in rad/m, is the spatial oscillation angular frequency and corresponds to a spatial oscillation period of $2\pi/\kappa$. When $A = 1$ and $\kappa = 0$, Eq. (11) reduces to the single-exponential form. Therefore, the exponential–cosine model retains the conventional exponential-decay behavior while providing additional flexibility to represent spatial coherence oscillations.

Spatial coherence oscillations mainly arise from interference among waveguide modes and multipath arrivals with different horizontal wavenumber projections onto the array axis. The phase differences among these components vary with inter-element separation, producing alternating constructive and destructive interference and thus an oscillatory spatial coherence pattern. Accordingly, κ represents the effective dominant spatial angular frequency of the modal and multipath interference pattern, with a corresponding spatial period of $2\pi/\kappa$. It is related to differences among the projected horizontal wavenumbers of the contributing components. It is also affected by their amplitudes and arrival directions, as well as by coupling among the contributing modes. Because the received field contains multiple interacting components, κ should be interpreted as an effective parameter characterizing the dominant projected-wavenumber structure rather than as the horizontal wavenumber of a single mode. Changes in water depth may modify the local modal structure, while 3D propagation and mode coupling may alter the arrival directions and relative modal energies of the contributing components. These changes may lead to variations in the fitted κ.

After substituting Eq. (11) into Eq. (10), the equation of array gain is written as

$$\mathrm{AG} = 10\lg(G_{\mathrm{inc}} + G_{\mathrm{coh}}), \quad (12)$$

where G_{inc} and G_{coh} denote the incoherent and coherent components of the linear array gain, respectively. The incoherent component G_{inc} is expressed as

$$G_{\mathrm{inc}} = \frac{1-A}{E_{\mathrm{tot}}}\left(\sum_{i=1}^{N}\sqrt{E_i}\right)^2, \quad (13)$$

and the coherent component G_{coh} is given by

$$G_{\mathrm{coh}} = \frac{A}{E_{\mathrm{tot}}}\sum_{i=1}^{N}\sum_{n=1}^{N}\exp(-\gamma\Delta r_{in})\cos(\kappa\Delta r_{in})\sqrt{E_i E_n}, \quad (14)$$

where G_{inc} corresponds to the non-oscillatory component associated with the constant term $(1-A)$ in the spatial coherence model. It is jointly determined by the weighting factor $(1-A)$ and the element energy distribution. The component G_{coh} represents the distance-dependent coherent contribution and is jointly governed by the coherent amplitude coefficient A, the spatial coherence attenuation coefficient γ, the spatial oscillation angular frequency κ, the inter-element separations Δr_{in}, and the element energy distribution. It should be emphasized that G_{inc} and G_{coh} are additive only in the linear domain, whereas the array gain in decibels is obtained after their linear summation according to Eq. (12).

The coherent amplitude coefficient A is the linear weight of the coherent term and determines the relative contributions of the coherent and incoherent components. The coefficient A only scales the overall amplitude of the spatial coherence curve without changing its oscillation structure or attenuation characteristics. The coherence attenuation coefficient γ controls the decay rate of the coherent envelope via the exponential term. It only changes the coherent amplitude without reversing the sign of coherent contributions. Its effect is strongly distance-dependent and is exponentially amplified in large-aperture arrays. The spatial oscillation angular frequency κ governs the spatial oscillation pattern of coherence via the cosine term. As κ increases, the oscillation period shortens, and the total coherent amplitude drops sharply.

To quantify variations in the element-energy distribution, two dimensionless coefficients are defined. The sound-field deviation coefficient ξ characterizes the relative difference between the element-energy distributions predicted by the 3D FE model and obtained from the experimental measurements. It is defined as

$$\xi = \frac{\sum_i \left|E_i^{\mathrm{3D}} - E_i^{\mathrm{real}}\right|}{\sum_i \left|E_i^{\mathrm{real}}\right|} \times 100\%, \quad (15)$$

where E_i^{3D} and E_i^{real} denote the element energies at the i-th array element predicted by the 3D FE model and obtained from the experimental measurements, respectively. A smaller value of ξ indicates closer agreement between the modeled and measured distributions.

The energy uniformity coefficient η quantifies the uniformity of the element-energy distribution along the horizontal array. It is defined as

$$\eta = \frac{\left(\sum_{i=1}^{N}\sqrt{E_i}\right)^2}{N\sum_{i=1}^{N}E_i}, \quad (16)$$

where E_i, i and N have the same meanings as defined previously. A value closer to unity indicates a more uniform element-energy distribution, whereas a smaller value indicates greater energy nonuniformity and a more pronounced energy offset along the array.

4. Simulation analysis

As derived in Section 3, array gain is jointly determined by the spatial coherence of the signal field and the amplitude distribution across array elements. For large-aperture horizontal arrays in continental slope environments, 3D acoustic propagation effects significantly influence both of these key factors and thus must be fully considered. This section quantitatively analyzes array gain degradation in slope environments, which helps systematically investigate the impacts of 3D propagation characteristics on signal spatial coherence and element energy distribution.

4.1. Fitting of spatial correlation parameters

To systematically assess the individual contributions in continental-slope environments, the spatial correlation functions derived from measured and simulated acoustic fields were fitted to the exponential–cosine coherence model. Based on the fitted parameters, the controlled-variable method was employed for the analysis.

To quantify the impact of 3D propagation characteristics on array gain, the measured data from Site S1 are selected for analysis. The coherence-model parameters obtained from the numerical models are compared with those fitted from the field measurements. The influence of 3D propagation characteristics on array gain is then analyzed. Based on the established exponential–cosine spatial coherence model, we perform nonlinear least squares fitting on the spatial coherence coefficients from measured data, the model with the effect of horizontal sound propagation, and the model without it, respectively. The core fitted parameters of the model are summarized in Table 2. To quantify the agreement between the fitted coherence model and the measured data, the sum of squared errors (SSE) is defined as

$$\mathrm{SSE} = \sum_{i=1}^{N} \left|\rho_{\mathrm{real}}(\Delta r_i) - \rho_{\mathrm{fit}}(\Delta r_i; A, \gamma, \kappa)\right|^2 \Big/ \sum_{i=1}^{N} \left|\rho_{\mathrm{real}}(\Delta r_i)\right|^2. \quad (17)$$

Table 2 summarizes the fitting results of the exponential–cosine spatial coherence model at Site S1. The 3D finite element model exhibits significantly better agreement with the experimental measurements than the $N\times$2D model. The $N\times$2D approximation neglects the horizontal bending of sound rays induced by continental slope bathymetry, which leads to significant discrepancies between the fitted parameters and field measurements. This approximation erroneously overestimates the spatial wavenumber difference between multipath arrivals, which results in an overpredicted spatial oscillation angular frequency κ. In addition, neglecting the effect of horizontal acoustic energy spreading leads to a significant underestimation of the spatial coherence attenuation coefficient γ. The 3D FE model explicitly incorporates 3D propagation effects. Consequently, the model correctly captures the multipath geometric relationship and the horizontal energy spreading mechanism. This feature results in more accurate values of γ and κ, as evidenced by the SSE of 0.0150 for the 3D FE model shown in Table 2.

Table 2. Fitting results of the spatial coherence model at Site S1.

Fitting data	Coherent amplitude coefficient A	Spatial coherence attenuation coefficient γ (m^{-1})	Spatial oscillation angular frequency κ (rad/m)	Spatial oscillation period T (m)	SSE
Experiment	0.9175	0.0200	0.1689	37.2006	–
3D	0.9200	0.0100	0.2000	31.4159	0.0150
$N\times$ 2D	0.9730	0.0055	0.2200	28.5599	0.0343

Given that the 3D FE model provides more faithful representations of the acoustic energy distribution and the spatial coherence characteristics of the noise field, adopting the 3D FE model for the subsequent array gain simulation studies is highly appropriate.

To further visualize and compare the performance of different models in reproducing the spatial coherence structure of the sound field, the fitting curves of the spatial coherence model are presented in Fig. 9. The dominant oscillation periods, calculated by $2\pi/\kappa$ from the fitted κ values, are also marked in Fig. 9.

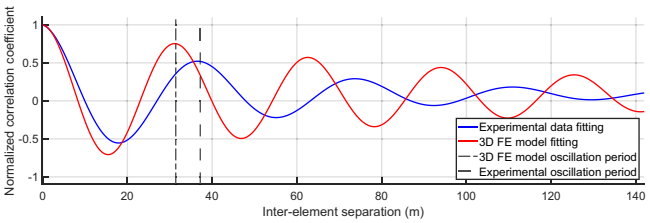

Fig. 9. Normalized spatial coherence function fitting curves based on the exponential–cosine model at Site S1. The blue and red solid lines represent the fitting results of the measured array data and the 3D FE model sound field, respectively. The two vertical dashed lines indicate the corresponding spatial oscillation periods of the coherence function for each case.

As shown in Fig. 9, the curve derived from the parameters fitted to the experimental data exhibits the longest spatial oscillation period (37.2 m) and the steepest attenuation with increasing inter-element spacing, with approximately four complete coherence oscillation cycles occurring across the 142.2 m array aperture. By comparison, the curve generated from the 3D FE model fitting parameters shows a slightly shorter spatial oscillation period (31.4 m) and a marginally slower attenuation rate, resulting in about four and a half cycles over the same array aperture. Despite these minor quantitative differences, the 3D FE model curve exhibits excellent overall agreement with the experimental fitting results. As a result, the characteristic damped oscillatory decay behavior of the spatial coherence observed in the field is accurately reproduced.

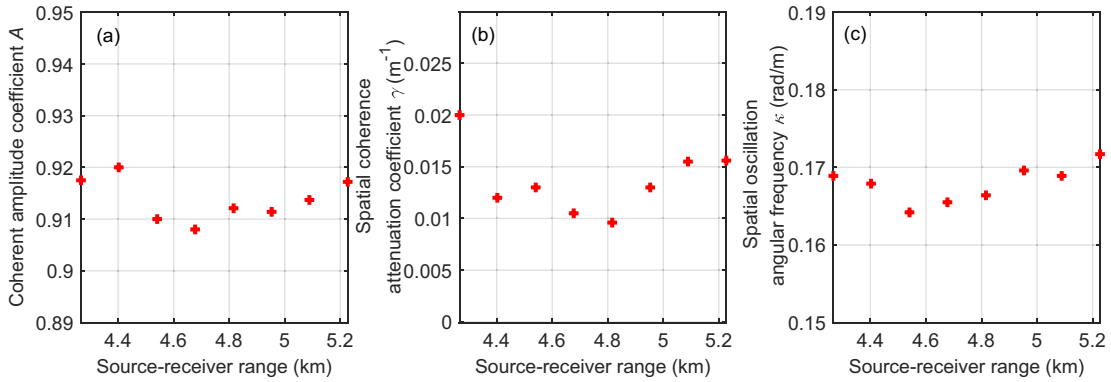

Fig. 10. Variations in the experimentally fitted spatial coherence parameters with source–receiver range across the eight measurement sites. (a) Coherent amplitude coefficient A. (b) Spatial coherence attenuation coefficient γ. (c) Spatial oscillation angular frequency κ. Each marker represents the fitting result obtained independently at one measurement site.

To characterize the variations in the spatial coherence parameters over the entire study area, the exponential–cosine model was independently fitted to the experimental data from Sites S1–S8. Figure 10 presents the fitted parameters as functions of source–receiver range. Over the range of 4.266–5.227 km, the coherent amplitude coefficient A varies from 0.9080 to 0.9200, with a mean value of 0.9137. The spatial coherence attenuation coefficient γ ranges from 0.0096 to 0.0200 m^{-1}, with a mean value of 0.0137 m^{-1}, whereas the spatial oscillation angular frequency κ ranges from 0.1642 to 0.1717 rad/m, with a mean value of 0.1679 rad/m.

As shown in Fig. 10(a), A exhibits relatively small, non-monotonic variations across the eight sites. Fig. 10(b) shows an overall decrease in γ from Site S1 to S5, despite a slight local increase at Site S3, followed by a steady increase from S5 to S8. Similarly, κ decreases from Site S1 to S3 and then shows an overall increasing trend toward Site S8, with a slight fluctuation at Site S7, as shown in Fig. 10(c). None of the three parameters exhibits a strictly monotonic dependence on source–receiver range. Their site-to-site variations may reflect the combined effects of propagation range, local bathymetry, multipath structure, and receiving-array position.

Despite these site-to-site variations, the three fitted parameters remain within bounded ranges throughout the study area. The following controlled-variable analysis examines whether their respective effects on array gain remain consistent across the eight sites.

4.2. Effects of spatial coherence parameters on array gain

The fitting results in Table 2 show that neglecting 3D propagation characteristics causes systematic deviations in all three core parameters of the spatial coherence model in wedge-shaped water environments, namely the coherent amplitude coefficient A, the spatial coherence attenuation coefficient γ, and the spatial oscillation angular frequency κ. To elucidate the underlying physical mechanism for how the spatial coherence structure governs the array gain of large-aperture horizontal arrays, this study employs a single-factor controlled-variable approach. Based on experimental measurements from a representative site, the controlled-variable analysis isolates and quantifies the individual impact of each core parameter (A, γ, and κ) on the shape of the spatial coherence function and the resulting array gain.

All simulations in this section employ the same array configuration as the experiment: an aperture of 142.2 m comprising 84 hydrophones. To isolate the effect of spatial coherence on array gain, all computations use the experimentally measured element energy E_i. Firstly, the parameters γ and κ are fixed at the fitted values of the measured spatial coherence data, which eliminates any confounding influence from modeling uncertainties in these parameters. Under this controlled condition, the coherent amplitude coefficients A derived from the measured data and the 3D FE model are separately substituted into the spatial coherence function. Moreover, the corresponding array gains are calculated. The results are shown in Fig. 11.

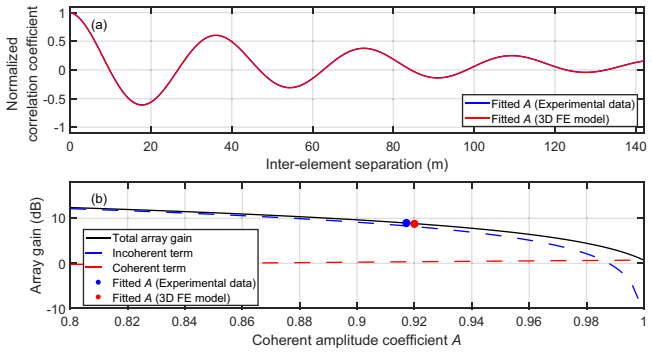

Fig. 11. Influence of the coherent amplitude coefficient A on the spatial coherence function and array gain. (a) Normalized spatial coherence coefficient as a function of the inter-element separation, which is calculated by substituting A values fitted independently from the measured data and the 3D FE model, with γ and κ fixed at the fitted values of the measured spatial coherence data. (b) Variations in total array gain, coherent term, and incoherent term with A. The blue and red dots mark the total array gain values corresponding to the two A values presented in panel (a).

As shown in Fig. 11(a), with γ and κ fixed, the spatial coherence curves exhibit distinct differences in envelope am-

plitude when using the coherent amplitude coefficient A predicted by different models, and this difference is positively correlated with the magnitude of A. The two curves have consistent zero-crossing positions and overall attenuation slopes, differing only in their oscillation envelope amplitudes.

Figure 11(b) further establishes the relationship between the coherent amplitude coefficient A and the array gain. Decomposition analysis shows that for large-aperture horizontal arrays, the contribution of the coherent component to the total array gain becomes negligible when the array aperture is much larger than the spatial coherence length. Consequently, array performance is governed nearly exclusively by the incoherent component. The 3D FE model correctly reproduces the horizontal diffusion of acoustic energy induced by continental slope topography. The horizontal acoustic energy diffusion degrades spatial coherence and results in a reduced coherent amplitude coefficient A. As shown in Fig. 11(b), the A values fitted from the experimental data and the 3D FE model yield array gain results that are consistent with field measurements. This agreement supports the conclusion that the reduction in A increases the weight of the incoherent term. This simulation result further validates that array gain is dominated by the incoherent component for large-aperture arrays in slope environments. Notably, the total array gain decreases nonlinearly with increasing A, and the rate of decrease becomes more pronounced at higher A values, as clearly illustrated by the black curve in Fig. 11(b).

To further investigate the influence of the spatial coherence attenuation coefficient γ on array gain, we fix the coherent amplitude coefficient A and the spatial oscillation angular frequency κ to the fitted values from the measured spatial coherence data. This procedure fully eliminates the confounding effects of the two parameters on the results. With A and κ fixed, we substitute the γ values fitted from the measured data and predicted by the 3D FE model into the spatial coherence function. We also calculate the discrepancies in the spatial coherence function and array gain caused solely by the variation in γ. The controlled-variable analysis quantifies the role of γ in mediating the effect of 3D propagation characteristics on array gain, and the results are presented in Fig. 12.

As shown in Fig. 12(a), with A and κ held constant, the zero-crossing positions of the two spatial coherence curves are perfectly consistent, and the only differences lie in the attenuation rates of the coherence envelopes. Specifically, a larger value of γ leads to faster decay of the sound field coherence with inter-element spacing — and correspondingly, a more rapid decline in the oscillation envelope. Quantitative fitting results confirm that 3D propagation effects strongly influence the spatial coherence attenuation coefficient γ. The 3D FE model accurately reproduces the attenuation characteristics observed in the experimental measurements.

Figure 12(b) reveals that the spatial coherence attenuation coefficient γ has a fundamentally different impact on array gain compared with the coherence amplitude coefficient A. Decomposition analysis further demonstrates that the incoherent component of array gain remains virtually invariant with γ, and any change in total array gain arises exclusively from variations in the coherent component. For large-aperture horizontal arrays dominated by the incoherent component, array gain exhibits extremely low sensitivity to γ. As shown in Fig. 12(b), the total array gain values corresponding to the γ values fitted from the experimental data and the 3D FE model are nearly identical. The total variation remains below 0.4 dB over the entire investigated parameter range.

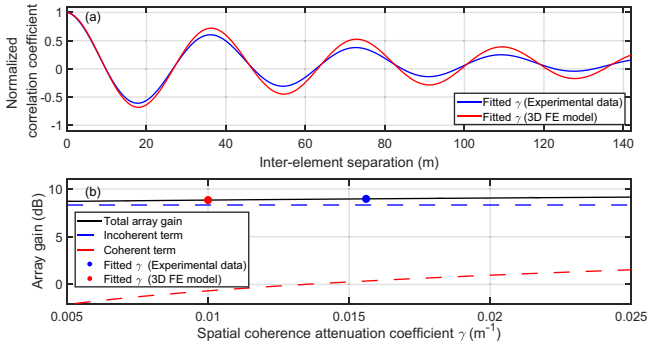

Fig. 12. Influence of the spatial coherence attenuation coefficient γ on the spatial coherence function and array gain under controlled conditions. (a) Normalized spatial coherence coefficient as a function of the inter-element separation, which is calculated by substituting γ values fitted independently from the measured data and the 3D FE model, with A and κ fixed at the fitted values of the measured spatial coherence data. (b) Variations in total array gain, coherent term, and incoherent term with γ. The blue and red dots mark the total array gain values corresponding to the two γ values presented in panel (a).

Building on the analysis of the coherent amplitude coefficient A and the spatial coherence attenuation coefficient γ, we next examine the influence of the spatial oscillation angular frequency κ using the same controlled-variable approach. The parameters A and γ are fixed at the values fitted from the measured spatial coherence data. This approach isolates the influence of κ and eliminates the confounding effects of the two parameters on the results. Next, the κ values fitted from the experimental data and the 3D FE model are separately substituted into the spatial coherence function. The resulting differences in array gain are then calculated to isolate the influence of κ. This analysis quantifies the contribution of the κ parameter to the array gain variation, and the results are presented in Fig. 13.

As shown in Fig. 13(a), with A and γ fixed at the values fitted from the experimental data, the two spatial coherence curves exhibit distinct differences primarily in their oscillation periods and nodal positions. A smaller κ value results in a longer oscillation period of the spatial coherence curve and a greater separation between adjacent peaks and troughs. Conversely, a larger value of κ leads to a shorter oscillation period

and a greater number of oscillations within the array aperture. As observed in Fig. 13(a), the 3D FE model yields a slightly larger κ value than that fitted from the experimental data. The larger κ value results in a marginally shorter oscillation period, consistent with the corresponding spatial coherence curve.

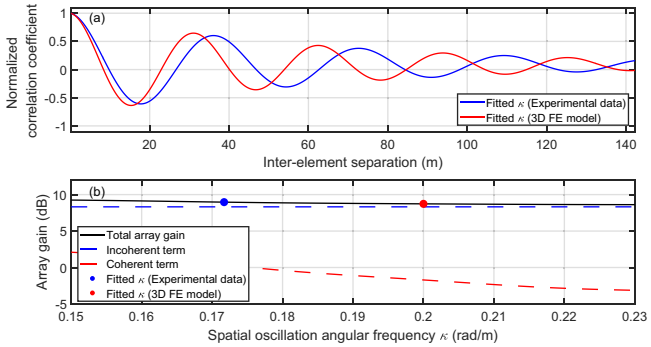

Fig. 13. Influence of the spatial oscillation angular frequency κ on the spatial coherence function and array gain under controlled conditions. (a) Normalized spatial coherence functions versus inter-element separation, calculated using κ values fitted from the measured data and the 3D FE model, respectively, with A and γ fixed at the values fitted from the measured spatial coherence data. (b) Variations in total array gain, coherent term, and incoherent term with κ. The blue and red dots mark the total array gain values corresponding to the two κ values presented in panel (a).

Figure 13(b) further illustrates the influence of the spatial oscillation angular frequency κ on array gain. The incoherent term remains nearly unchanged with κ. The slight decrease in the total array gain is mainly caused by the coherent term. Within the κ range investigated in this study (0.15–0.23 rad/m), the total array gain varied by less than 0.56 dB. The total array gain values corresponding to the κ values fitted from the experimental data and the 3D FE model are nearly identical. The array-gain variation of less than 0.56 dB demonstrates that the total array gain is relatively insensitive to moderate variations in κ. Therefore, changes in the spatial coherence oscillation pattern have only a limited influence on the overall array gain of large-aperture horizontal arrays. By comparison, the dominant spatial coherence parameter affecting array gain is the coherent amplitude coefficient A.

Controlled-variable simulations presented in Figs. 11–13 quantitatively isolate the individual pathways through which 3D acoustic propagation affects array gain. Array gain decreases by 3.57 dB solely due to the change in the coherent amplitude coefficient A. This reduction accounts for over 85% of the total array gain degradation. By contrast, the effects of γ and κ are relatively weak.

The above controlled-variable analyses reveal that A has a substantially stronger influence on array gain than γ and κ. To further clarify the mechanism underlying the dominance of the incoherent component in the array gain of the large-aperture horizontal array, the coherent and incoherent components in Eqs. (13) and (14) are calculated as functions of array aperture, as shown in Fig. 14(a). Since these two components are additive only in the linear domain, their percentage contributions to the total linear array gain are defined as

$$C_{\mathrm{inc}} = \frac{G_{\mathrm{inc}}}{G_{\mathrm{inc}} + G_{\mathrm{coh}}} \times 100\%,$$
$$C_{\mathrm{coh}} = \frac{G_{\mathrm{coh}}}{G_{\mathrm{inc}} + G_{\mathrm{coh}}} \times 100\%, \tag{18}$$

where C_{inc} and C_{coh} denote the percentage contributions of the incoherent and coherent components, respectively, and satisfy $C_{\mathrm{inc}} + C_{\mathrm{coh}} = 100\%$. The variations in C_{inc} and C_{coh} with array aperture are presented in Fig. 14(b).

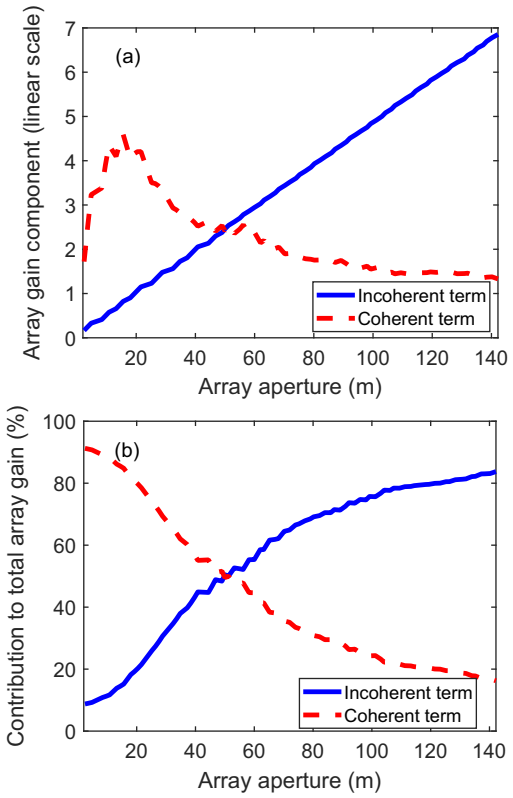

Fig. 14. Variation in the coherent and incoherent components with array aperture at Site S1 in the wedge-shaped slope environment. The array aperture denotes the distance from the first array element to the last included array element. (a) Coherent and incoherent components of array gain presented on a linear scale. (b) Percentage contributions of the coherent and incoherent components to the total linear array gain.

As shown in Fig. 14(a), the coherent component initially increases with array aperture, reaches a maximum at approximately 15–20 m, and then decreases overall, whereas the incoherent component increases continuously. Figure 14(b) shows that the contribution of the incoherent component increases with array aperture, whereas that of the coherent component decreases. At the full aperture of 142.2 m, the two components account for approximately 84% and 16% of the total linear array gain, respectively, confirming the dominance of the incoherent component at large apertures.

According to Eqs. (13) and (14), the coherent and incoherent components exhibit different dependencies on array aperture. For a small aperture, most element pairs are closely spaced. Consequently, the exponential attenuation factor $\exp(-\gamma\Delta r_{in})$ remains close to unity, while the cosine terms

$\cos(\kappa\Delta r_{in})$ for most closely spaced element pairs have consistent signs. Therefore, the coherent component G_{coh} initially increases as the number of strongly correlated element pairs increases. As the array aperture increases, the number of widely separated element pairs gradually increases. For these element pairs, the exponential term $\exp(-\gamma\Delta r_{in})$ reduces the magnitude of their coherent contributions, while the term $\cos(\kappa\Delta r_{in})$ changes sign with element separation, causing positive and negative contributions to partially cancel. Consequently, the coherent component reaches a maximum and then decreases overall. In contrast, G_{inc} contains neither the distance-dependent attenuation nor the oscillatory factor, and its same-sign contributions accumulate without spatial cancellation. Therefore, the incoherent component G_{inc} continues to increase with array aperture and eventually becomes the dominant contribution to the total array gain.

To examine the generalizability of the conclusions from the previous single-site analysis, eight sites at different distances in the wedge-shaped environment were further analyzed. The same controlled-variable method was adopted to quantify the independent effects of three core spatial coherence parameters on the array gain of large-aperture horizontal arrays across different measurement sites. The results are presented in Fig. 15.

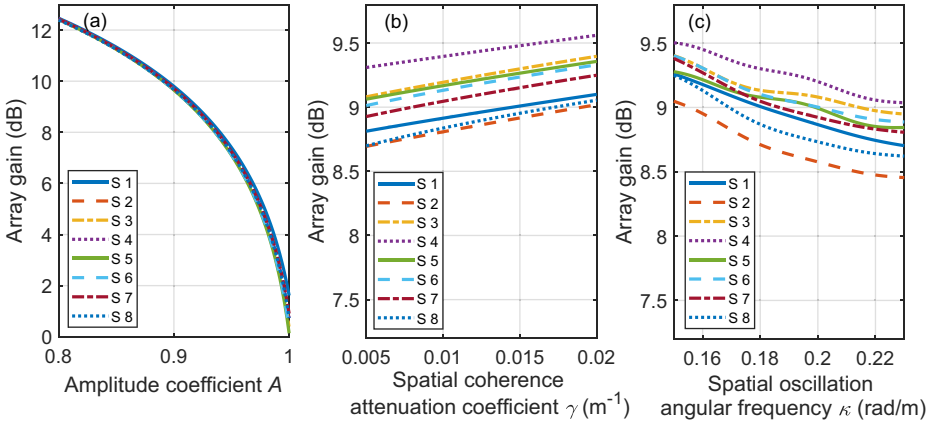

Fig. 15. Comparison of the independent effects of the three spatial coherence parameters on array gain at different sites in the wedge-shaped environment. (a) Variation of array gain with the coherent amplitude coefficient A. (b) Variation of array gain with the spatial coherence attenuation coefficient γ. (c) Variation of array gain with the spatial oscillation angular frequency κ. The same controlled-variable method is applied to all eight sites: when evaluating the effect of a single parameter, the other two parameters are fixed at their respective fitted values obtained from the measured data at the corresponding site.

Figure 15(a) clearly demonstrates that the dominant influence of the coherent amplitude coefficient A on array gain is highly generalizable across the eight sites. The array gain curves for the eight sites nearly overlap and all exhibit a consistent monotonic decrease with increasing A. Within the typical operating range of the wedge-shaped slope environment investigated in this study, the array gain at all sites varies by more than 12 dB as the parameter A increases from 0.8 to 1.0. The array-gain variation induced by A is substantially greater than the combined effects of the other two parameters, γ and κ. Figures 15(b) and 15(c) further demonstrate that the spatial coherence attenuation coefficient γ and the spatial oscillation angular frequency κ have consistently weak effects on array gain across all eight sites. The small array-gain variations indicate that the influences of γ and κ are relatively insensitive to site-to-site environmental differences. Specifically, as shown in Fig. 15(b), when γ varies within the range of 0.005–0.025 m^{-1}, the resulting change in array gain remains below 0.8 dB for every site. Similarly, as shown in Fig. 15(c), over the investigated range of κ (0.15–0.23 rad/m), the array gain variation is uniformly less than 0.6 dB across all sites. This small variation confirms that κ exerts the weakest influence among the three spatial coherence parameters. The consistent parameter-sensitivity trends across the eight sites support the applicability of the proposed relationship between 3D propagation and array gain within the investigated wedge-shaped slope region. Despite variations in propagation distance and receiving depth, the coherent amplitude coefficient A remains the dominant factor, whereas the effects of γ and κ remain relatively weak.

4.3. Effects of element energy on array gain

The effects of the three core spatial coherence parameters (A, γ, and κ) on array gain have been systematically quantified, and the consistency of their influence trends across multiple sites has been confirmed. The independent contribution of element energy E_i to array gain was then isolated. For each site, the controlled-variable method was employed by fixing the spatial coherence parameters A, γ, and κ at the values fitted from the corresponding measured data. Fixing these parameters eliminates their influence on the analysis of element energy.

The element energy E_i was then varied, and the effects of the E_i values obtained from the measured data and the 3D FE model on array gain were compared. The comparison results

are shown in Fig. 16.

Figure 16(a) presents the sound-field deviation coefficients ξ calculated using the 3D FE model across the eight measurement sites. The sound-field deviation coefficients range from 0.128 to 0.261 across the eight sites, indicating relatively weak spatial nonuniformity within the investigated wedge-shaped slope region. Figure 16(b) compares the energy uniformity coefficients η obtained from the experimental measurements and the 3D FE model. The 3D FE model accurately reproduces the site-to-site variations observed in the experimental data. The experimental and model-derived curves exhibit similar trends across all eight sites.

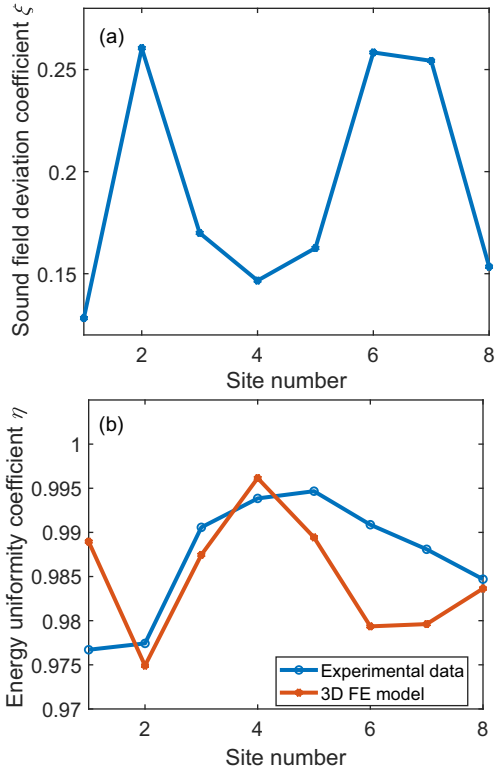

Fig. 16. Comparison of element-energy characteristics between the experimental measurements and the 3D FE model at eight measurement sites in the wedge-shaped slope region. (a) Sound-field deviation coefficient ξ calculated using the 3D FE model. (b) Energy uniformity coefficient η obtained from the experimental measurements and the 3D FE model.

The physical reason for these subtle energy variations is that, even when the array aperture is much smaller than the propagation distance, the horizontal spreading of acoustic energy induced by continental slope bathymetry still introduces measurable differences among adjacent array elements. By explicitly accounting for 3D propagation effects, the 3D FE model resolves the fine-scale variations in the element-energy distribution.

To isolate and quantify the influence of element signal-energy distribution on array gain performance, a controlled-variable method was employed. For each of the eight measurement sites, the spatial coherence parameters A, γ, and κ were fixed at their site-specific values obtained from the experimental measurements. The element signal energies E_i obtained from the experimental measurements and the 3D FE model were then used separately to calculate the array gain. The resulting array-gain variations are shown in Fig. 17.

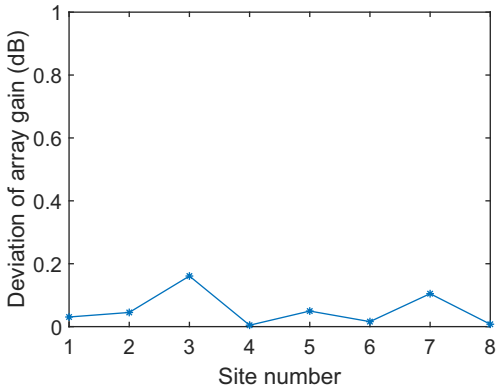

Fig. 17. Array-gain deviations induced solely by element-energy prediction errors at eight measurement sites in the wedge-shaped slope region. The model array gain is calculated using Eq. (12). The deviations are calculated as the absolute differences between array gains obtained using the measured element energy and the 3D model-derived element energy. In this controlled-variable analysis, all spatial coherence parameters (A, γ, and κ) are fixed at their experimentally measured values to isolate the independent contribution of element-energy errors.

Across all sites, the array gain deviations caused by using the measured and 3D model-derived element energies remain below 0.16 dB. This result demonstrates that, for the wedge-shaped shallow-water environment and large-aperture horizontal array configurations investigated in this study, variations in the element signal energy distribution have a negligible impact on array gain performance. The element-energy distribution predicted by the 3D FE model exhibits only minor deviations from the experimental measurements. Nevertheless, the measured and model-derived element energies yield nearly identical array gain results when the same spatial coherence parameters are used. The close agreement between the two array gain results indicates that spatial coherence characteristics, rather than the element signal energy distribution, are the dominant factor determining array gain performance in continental slope environments.

Based on the coherence-parameter analysis in Subsection 4.2 and the element-energy analysis presented above, the findings regarding the influence of 3D propagation on array gain can be summarized as follows. In the wedge-shaped slope environment, bathymetry-induced 3D propagation modifies the spatial coherence and element-energy distribution of the received field along the horizontal array. Among the fitted coherence parameters, variations in A have the strongest effect on array gain under the investigated conditions. This is because A determines the relative contributions of the damped oscillatory and nonoscillatory coherence components. By comparison, γ controls the distance-dependent attenuation of the coherent contributions, whereas κ governs their spatial oscillations and

associated cancellation effects. Consequently, their net effects on array gain are less pronounced under the investigated conditions. Meanwhile, variations in the element-energy distribution affect the contributions of different element pairs to the beamformer output, thereby influencing the array gain. Together, changes in spatial coherence and element-energy distribution represent two important pathways through which 3D propagation influences array gain.

4.4. Measured array gain verification

The spatial coherence model developed in this study provides a physical interpretation that links complex underwater propagation effects to spatial coherence characteristics and ultimately to array gain performance. This interpretation reveals that 3D propagation effects reduce the coherence amplitude coefficient A, which is the dominant factor determining array gain performance in continental slope environments. To quantitatively evaluate the prediction error of the 3D FE model for array gain, the normalized mean squared error (NMSE) for each measurement site is defined as

$$\mathrm{NMSE} = \frac{\|AG_{\mathrm{real}} - AG_{\mathrm{3D}}\|_2^2}{\|AG_{\mathrm{real}}\|_2^2}. \tag{19}$$

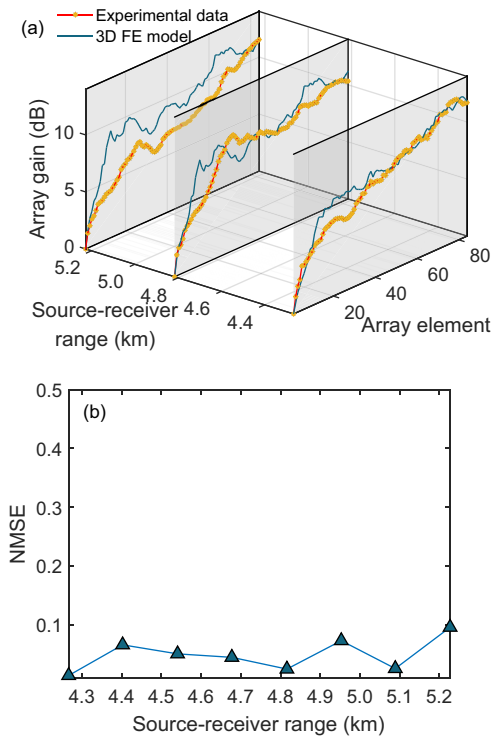

Fig. 18. (a) Comparison of array gains calculated from the experimental data and the 3D FE model for different source–receiver ranges and numbers of array elements. The source–receiver range denotes the distance between the acoustic source and the receiving array. The red curve represents the experimental data, and the blue curve represents the array gain calculated from the 3D FE model; (b) NMSE between the measured and 3D FE model-predicted array gains.

Figure 18(a) compares the array gain results calculated using the 3D FE model with the experimental measurements across different receiving ranges and numbers of array elements. The results from the 3D FE model agree well with the experimental data. Thus, the variation trends of array gain with propagation range and array aperture are accurately reproduced.

Figure 18(b) further demonstrates the consistency between the theoretical calculations and field measurements across all investigated receiving ranges. Calculations that account for 3D acoustic propagation characteristics yield NMSE values below 0.08 at all sites, indicating excellent and stable agreement with the experimental observations. These results further confirm the consistency between the theoretical analysis presented in this paper and the experimental data.

5. Conclusion

This study investigates the influence of 3D acoustic propagation characteristics on array gain performance in wedge-shaped slope environments. The derivation of an array gain calculation formula based on the exponential–cosine spatial coherence model provides a clear physical interpretation of the effects of 3D propagation on spatial coherence and array gain.

In range-dependent slope environments, 3D propagation characteristics affect large-aperture array gain primarily by redistributing energy between coherent and incoherent field components. Using a rigorous controlled-variable method, we quantitatively isolated the independent contributions of the three core spatial coherence parameters (the coherent amplitude coefficient A, the spatial coherence attenuation coefficient γ and the spatial oscillation angular frequency κ) and the array element energy E_i to the total array gain. Furthermore, the underlying physical relationship between 3D propagation characteristics and the array gain of large-aperture arrays was established. Specifically, incomplete accounting for 3D propagation effects leads to an overestimation of the coherence amplitude coefficient A, which in turn results in an underestimation of array gain.

Based on sound propagation data collected at eight sites in the slope region of the South China Sea in 2025, the array gains calculated using the 3D FE model agree closely with those derived from the experimental measurements, with NMSE values below 0.08 at all measurement sites. This cross-site agreement provides experimental support for the model-predicted array-gain behavior described above and supports the reliability of the 3D FE model within the investigated study area. The agreement is also consistent with the proposed physical interpretation linking 3D sound propagation, spatial coherence, and array gain. This work provides valuable insights into the design and performance evaluation of sonar arrays in continental slope environments.

Acknowledgments

Project supported by the National Natural Science Foundation of China (Grant Nos. 52571391 and 12274347) and the Stable Supporting Fund of Acoustic Science and Technology Laboratory (Grant No. JCKYS2025SSJS009).

References

[1] Bourret R C 1961 *J. Acoust. Soc. Am.* **33** 1793
[2] Bordelon D J 1962 *J. Acoust. Soc. Am.* **34** 555
[3] Brown J L 1962 *J. Acoust. Soc. Am.* **34** 1927
[4] Kleinberg L I 1980 *J. Acoust. Soc. Am.* **67** 572
[5] Carey W M 1999 *Proceedings of the MTS/IEEE Oceans '97 Conference*, October 6–9, 1997, Halifax, NS, Canada, pp. 462
[6] Dong F C, Li Z L, Hu Z G and Wu S L 2022 *IEEE J. Ocean. Eng.* **47** 751
[7] Duda T F, Collis J M, Lin Y T, Newhall A E, Lynch J F and Deferrari H A 2012 *J. Acoust. Soc. Am.* **131** 1782
[8] Xie L, Sun C, Liu X H, Jiang G Y and Long D Z 2017 *Acta Phys. Sin.* **66** 194301 (in Chinese)
[9] Liu Z W, Yang C M, Jiang Y, Xie L, Du J Y and Lü L G 2021 *Appl. Sci.* **11** 5046
[10] Xie L, Sun C, Liu X H and Jiang G Y 2016 *Acta Phys. Sin.* **65** 144303 (in Chinese)
[11] Buckingham M J 1979 *J. Acoust. Soc. Am.* **65** 1551
[12] Hamson R M 1980 *J. Acoust. Soc. Am.* **68** 156
[13] Heaney K D 2011 *J. Acoust. Soc. Am.* **129** 2026
[14] Zavol'skii N A, Malekhanov A I, Raevskii M A and Smirnov A V 2017 *Acoust. Phys.* **63** 542
[15] Gao Y and Zheng G Y 2022 *Proceedings of the 3rd International Conference on Geology, Mapping and Remote Sensing*, April 22–24, 2022, Zhoushan, China, pp. 332
[16] Liu Q Y, Song J and Zhao C M 2010 *Acoust. Electron. Eng.* **2** 8
[17] Rouseff D and Lunkov A A 2015 *J. Acoust. Soc. Am.* **138** 2256
[18] Zhang B, Li F H, Li Z L, Zhang Y J and Wang J Y 2019 *MATEC Web Conf.* **283** 02001
[19] Orr M, Pasewark B, Wolf S, Lynch J and Chiu C 2003 *J. Acoust. Soc. Am.* **114** 2460
[20] Xie L and Sun C 2016 *Sci. Sin. Phys. Mech. Astron.* **46** 094308
[21] Lin Y T, Uffelen L J V, Miller J H, Potty G and Vigness-Raposa K J 2022 *J. Acoust. Soc. Am.* **151** 1684
[22] Gorodetskaya E Y and Malekhanov A I 1999 *IEEE J. Ocean. Eng.* **24** 156
[23] Mo Y X, Zhang C J, Lu L C, Sun Q H and Ma L 2024 *Chin. Phys. B* **33** 034301
[24] Xie L, Sun C and Kong D 2020 *IEEE Access* **8** 177437
[25] Su X X, Zhang R H and Li F H 2006 *Acta Acust.* **31** 305